Origin of high interfacial resistances in solid-state batteries: interdiffusion and amorphous film formation in LLTO/LMO half cells

Abstract:

The large interfacial resistance between electrolyte and electrode has become a significant roadblock for the commercialization of all-solid-state batteries. The formation of interfacial phases (interphases) has been considered as one of the most significant sources for such high resistance. Therefore, studying the mechanism of interphase formation, along with investigating its effect on ionic conductivity, could lead to the discovery of avenues towards designing high performance all-solid-state Li ion batteries. In this work, we studied the interphase formation in the perovskite electrolyte $Li_{0.33}La_{0.57}TiO_3$(LLTO) and spinel cathode $LiMn_2O_4$ (LMO) pair by co-sintering experiments via Spark Plasma Sintering (SPS), as well as conventional sintering. We observed that while the processing method has an influence on the quality of the electrode/electrolyte contact, the formation of an interphase could not be avoided. At the LLTO/ LMO interface, we observed both an interphase formed by interdiffusion, as well as a complexion-like amorphous layer. We directly characterized the complexion layer morphology via HRTEM. Analytical TEM and SEM where used to reveal the elemental composition of the interphase. Furthermore, we used impedance spectroscopy to measure the electrical properties of the LLTO/LMO interphase and identified the interfacial resistance from the interdiffusion induced interphase to be larger than the individual phases about by a factor of 40, while the amorphous layer was not visible in the impedance.

Introduction:

All-solid-state lithium ion batteries have been regarded as the most promising power source for electric vehicles (EVs)[1–3]. By replacing flammable organic liquid electrolytes with non-flammable solid electrolytes (SEs), solid state batteries (SSBs) are projected to solve the safety issues of traditional lithium-ion batteries.[4,5] Moreover, solid

electrolytes typically provide broader electrochemical windows, which could enable the application of higher potential cathodes. By suppressing the dendrite formation, SEs also make the use of lithium metal anodes possible in batteries[6,7], therefore increase the energy density of SSBs.

However, the poor ionic conductivity of SEs and the high interfacial resistance between SEs and electrodes are the two main drawbacks that could lead to low power density and poor cycling performance of SSBs.[8] Recently, great progress has been made in improving the ionic conductivity of SEs. Kanno's group reported a lithium superionic conductor $Li_{10}GeP_2S_{12}$ with ionic conductivity of 10^{-2} S/cm[9], which was comparable to a liquid electrolyte. At the same time, perovskite[10], NASICON-like[11] and garnet type[12] solid electrolytes were also reported to reach ionic conductivities of about 1mS/cm at the room temperature[13]. On the other hand, the large interfacial resistance between electrode and electrolyte could also lead to large internal resistance of the battery and result in a loss of energy density[14]. However, the interfacial phenomena between electrodes and electrolyte in SSBs still lacks a complete understanding. Formation of interelectrode films[15,16], space-charged layer effect[17,18] and the contact loss caused by the deformation of electrodes during cycling[19] are potential reasons for the large interfacial resistance. Among these, the interphase formation at the cathode/electrolyte interface during charging has been observed experimentally by Sakuda[20] and further theoretically testified by Ceder's group[6]. This interphase could significantly affect the charge transfer kinetics in the batteries and cost great ohmic loss. Studying the formation mechanisms of interphase and investigating its effect on ionic conductivity is the first step towards engineering structurally stable interfacial phases that maximize the interfacial conductivity can be very significant to SSBs.

Meanwhile, co-sintering experiments have been widely applied to investigate possible interfacial reactions between oxide electrolyte/electrode combinations[14,21–23], where the compatibility of garnet-like electrolyte[24] and Lithium Aluminum Titanium Phosphate (LATP)[14] against common cathode materials has been investigated. However, there is

still a lack of research in the compatibility of perovskite electrolytes against cathode materials. Interphase formation occurs during co-sintering by an interdiffusion process between both materials involved. Based on such experiments, this work evaluates the feasibility of a pair of model cathode/electrolyte ceramics for SSB applications. Lithium Lanthanum Titanite ($Li_{0.33}La_{0.57}TiO_3$, LLTO) is a perovskite electrolyte with a high bulk ionic conductivity of 10^{-3} S/cm at room temperature[10]. LLTO is stable in air and would not release any toxic gases as a result of breaking down as sulfide electrolyte[22]. In addition, LLTO has good high temperature stability and is reported to be stable against high voltage cathodes[25,26]. Therefore, LLTO is a promising SE candidate in SSBs. However, its high grain boundary resistance and instability against low potential anodes are challenges that LLTO would face as a solid electrolyte in a battery[27]. Lithium Manganese Oxide ($LiMn_2O_4$, LMO) is a popular spinel cathode material, and it has been considered as the best candidate replacing e.g. lithium cobalt oxide ($LiCoO_2$) because of the abundancy of manganese in nature and its low toxicity level.[28,29]

Spark plasma sintering (SPS) is an advanced sintering method that utilizes uniaxial pressure and a pulsed DC current to consolidate powders with high sintering rates[30]. As mechanical pressure adds to the driving force for sintering and direct heating allows for very high heating rates, lower process temperatures and shorter sintering time can be achieved, which can suppress particle coarsening greatly[31]. Particularly, the formation of interphase can be alleviated, which is beneficial for batteries. The possibility of applying SPS to produce a laminar cathode/electrolyte/anode SSB has been brought to light according to the time-saving and good interfacial contact promised by this technique[32,33].

As future SSBs need a functioning interphase layer without the development of large resistances, a careful choice of chemistries and processing parameters is needed. A computational study of the interphase formation will need experimental input on the interdiffusion and phases that are being formed in the contact area. So far, no

information is available for the interphase formation for the half-cell pair LLTO/LMO. Therefore, in this work, we co-sintered LLTO and LMO via both SPS and conventional sintering to understand their benefits as processing methods for the investigation of cathode/electrolyte interphase formation. Studies on the cathode/electrolyte compatibility via SPS provide critical information for the implementation of SPS to produce solid-state batteries. We used scanning Electron Microscopy (SEM), High Resolution Transmission Electron Microscopy (HRTEM), Scanning Transmission Electron Microscopy (STEM) and Energy Dispersive X-ray spectroscopy (EDS) as characterization methods of the cathode/electrolyte interphase. Additionally, we analyzed the effect of the interphase formation on the overall conductivity by Electrochemical impedance spectroscopy (EIS).

Experimental

Powder synthesis: $Li_{0.33}La_{0.57}TiO_3$ (LLTO) was synthesized by solid state reaction. Li_2CO_3 (Sigma-Aldrich), La_2O_3(Sigma-Aldrich) and TiO_2 (Rutile, Sigma-Aldrich) were mixed according to stoichiometry in an attrition mill. The mixed powders were then dried and calcined in a tube furnace at 1050°C for 6 hours to allow the solid state reaction to the perovskite phase. The LLTO powders were attrition milled again for 2 hours to break the agglomeration formed during calcination. The powder was characterized by XRD and SEM.

The cathode material, $LiMn_2O_4$ (LMO) is commercially available from Sigma Aldrich (>99%, <0.5 μm particle size).

Pellets for Sintering: LLTO and LMO powders were co-pressed axially into a layered pellet as shown in Figure 1 (a). LMO powders were pressed into a green pellet at 80 MPa for 1 minute. Subsequently, the same volume of LLTO powders were added and again pressed at 80MPa for 1 minute.

SPS and Conventional Co-sintering

Figure 1 (b) shows a co-pressed pellet sintered by a Thermal Technology SPS 10-3 machine. The SPS experiment was carried out at 50 MPa and 900℃ for 10 minutes. The heating and cooling rate were 100 °C/ min. The co-sintered pellet was then cut and embedded in epoxy. The cross-section was polished with SiC paper and diamond slurry (final particle size was 1μm).

Figure 1 (c) shows a co-pressed pellet after conventional sintering at 900°C in a tube furnace for 4 hours in Ar atmosphere. The pellet was cut and embedded in epoxy and the cross-section was polished similarly to the SPS sample.

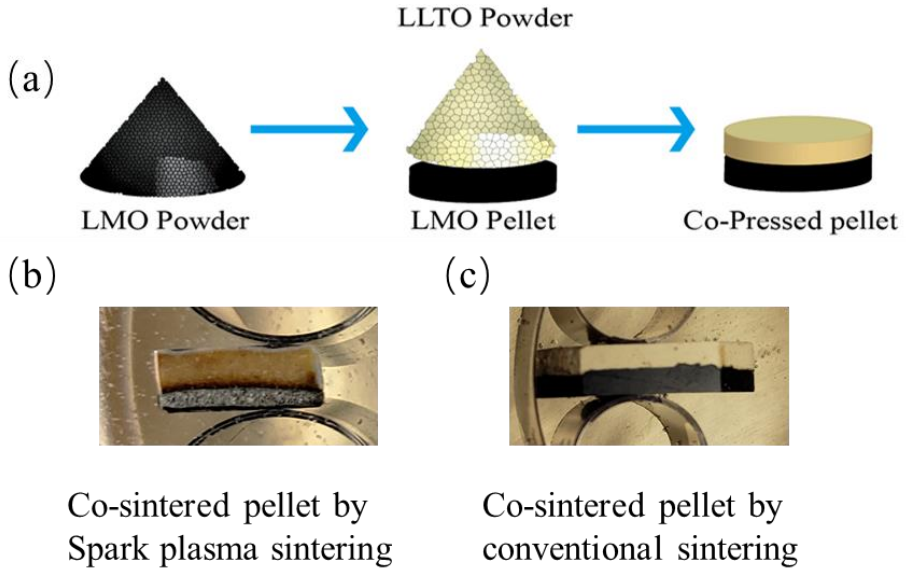

Figure 1 （a）Procedure for the fabrication of co-pressed pellets (b) co-pressed pellet sintered by spark plasma sintering (SPS), embedded in epoxy and polished. (c) co-pressed pellet sintered by conventional sintering, embedded in epoxy and polished

Materials Characterization

Scanning Electron Microscopy (SEM) and X-ray diffraction (XRD) were applied to characterize the LLTO powders. To evaluate the phases that might be formed by reactions between LLTO and LMO, the LLTO and LMO powders were mixed together at a volume ratio of 1:1 with a mortar and pestle. The mixture of electrolyte and cathode powders were then pressed into pellets under a pressure of 100MPa. Pellets were heated at 900° in Ar atmosphere for 4 hours. A subsequent XRD analysis has been applied to

the mixed pellet by a Bruker D8 Focus machine from 2θ =15° to 80° was applied to identify the resulting phases.

For all pellets prepared by conventional sintering and spark plasma sintering, microstructures of interfacial regions have been investigated by SEM (FEI Quanta 650). EDS mapping and line scans (EDAX and Oxford Instruments), have also been applied to detect elemental distribution in the interfacial region. For the SPS sintered pellets, the interfacial region (~ 10 μm) was cut and lifted out using a Focused Ion Beam microscope (FIB, FEI Quanta 3D). HRTEM, STEM and EDS have also been applied to characterize the microstructure and chemistry using a FEI Talos 200X TEM.

Electrochemical impedance spectroscopy (EIS) was applied to the SPS co-sintered pellet, a pure LLTO pellet and a pure LMO pellet to characterize the effect of interfacial layer on overall resistivity with a BioLogic electrochemistry potentiostat in the frequency range of 1MHz to 1Hz.

Results & Discussion

Powder characterization and phase composition

According to SEM images showed in Figure 2(a), the particle size of the powder precursors is about 500nm. The XRD spectrum of LLTO is shown in Figure 2 (b), and matches the standard PDF card JCPDS No.870935, which underlines the phase purity of the synthesized $Li_{0.33}La_{0.57}TiO_3$.

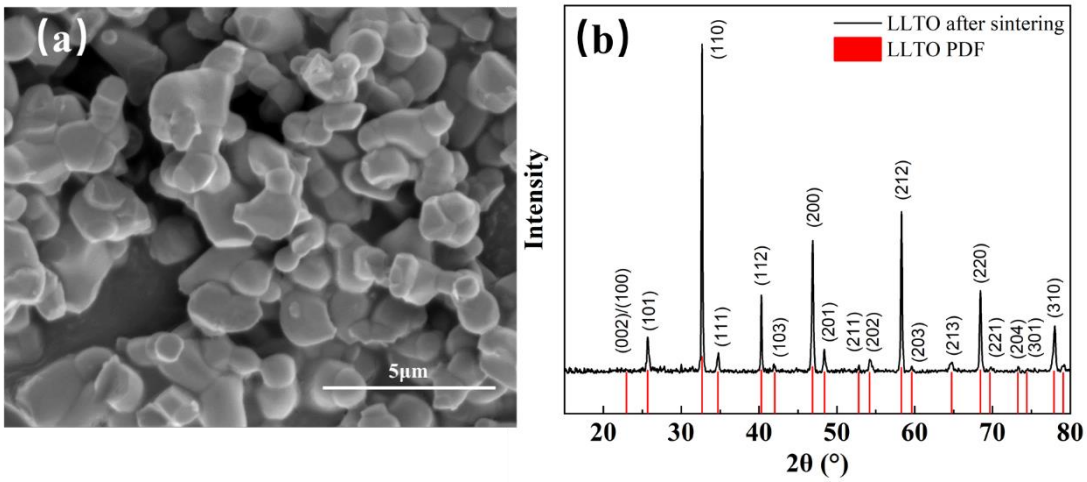

Figure 2 (a) SEM images of LLTO powders synthesized by solid state method, (b) XRD data of the LLTO powders compared with standard PDF card JCPDS No.870935

The XRD analysis of the individual LMO and LLTO, as well as the mixed LMO/LLTO pellets after heating to 900°C for 4h are shown in Figure 3. Comparing the pattern of the mixed pellet to the LLTO and LMO powders, no extra peak is visible in the mixed pellet profile, which indicates there is no significant chemical reaction or phase formation during conventional co-sintering of LLTO and LMO powders. However, this result does not indicate that there is no interphase formation at the interface between LLTO and LMO after sintering. Merely, the XRD results show that in each of the individual bulk phases, there are no phase transformations or chemical reactions that occur simply by heating the powders up to 900°C. A potential interphase formation would fall below the detection limit of the XRD.

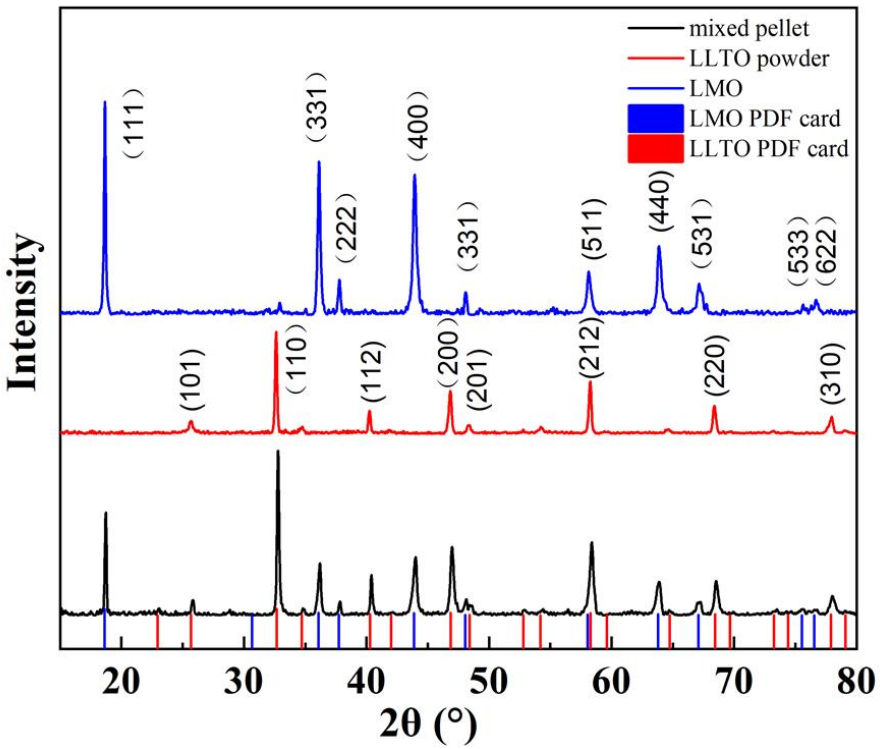

Figure 3 XRD patterns of $Li_{0.33}La_{0.57}TiO_3$ (LLTO), $LiMn_2O_4$(LMO), and LLTO+LMO powder mixture pellet heated to 900°C for 4h compared with standard PDF cards.

Electron Microscopy Characterization of Conventionally Sintered Sample

Analytical SEM and TEM has been widely applied in the investigation of interphases. Interdiffusion can be identified by the concentration gradient in element distribution profile[34]. In solid state batteries, Han[19] successfully observed an interphase formed by interdiffusion between LCO and LLZO via SEM and EDS mapping, and Kim[35] detected the similar interdiffusion via TEM and EDS line scan. Moreover, in high resolution TEM or STEM, the interphase could be observed directly by the difference in atomic arrangement or atomic number(Z) contrast. Sakuda[20] observed a clear interphase formed between LCO and Li_2S-P_2S_5 via HAADF mode in STEM.

To investigate the impact of the sintering process, the conventionally sintered sample from Fig.1(c) was analyzed by SEM and EDS as shown in Fig.4. According to Fig.4 (a), conventionally sintering at 900℃ for 4 hours did not fully densify LLTO and LMO. The interfacial region also did not have a good contact, as we can see voids along the

interfacial region (in red circle). The SEM-EDS results in Fig.4 (c) indicated that significant interdiffusion between Mn and Ti element occurred in an about 20µm thick region, while same profile for La was much shorter (about 10µm). In Mn and Ti element mappings (Fig.4 (a)) we could see clear diffusion of Mn and Ti ions across the interface, however, in the La element mapping, the La concentration in the LMO was below the detection limit. This indicated that the La ions are much less involved in the interdiffusion process compared to Ti and Mn. However, as best illustrated by the high concentration of Mn on the left end of the linescan in Fig. 4 (c) (i.e. in the LLTO), the true diffusion distances for Mn, Ti and La ions are greater than the scanned length in Fig.4 (b). Therefore, line scans at boarder scales have been applied (Fig.S1 in supplementary information). The diffusion distances for Mn, Ti and La ions are about 300µm. However, we did not detect any evidence for a second phase formation within this interdiffusion layer.

Electron Microscopy Characterization of SPS Sample

We compared the SEM images of the cross-sections of SPS sintered LLTO/LMO and conventionally sintered LLTO/LMO (Fig 4.(a) and Fig 5.(a)). The interfacial regions were also investigated by EDS to analyze the interdiffusion of elements (Figures 4 and 5).

The SEM overview of the interfacial region of the SPS sample is shown in Fig. 4(a). The LLTO is on the left and LMO is on the right. Both materials were sintered to very high density (>98%). The interface between LLTO and LMO shows a roughly 5 µm thick intercalation layer. The interphase region was further investigated by the EDS line scan and mapping results in Fig.4 (b) and Fig.4 (c). In the EDS line scan profile in Fig.4 (b), concentration gradients were observed. This interdiffusion layer is about 20µm thick for Mn ions and more than 30µm for Ti ions as indicated by the red dashed lines. However, for La ions, only about 5µm (marked with blue dashed lines) of interdiffusion occurred. Given that at the interface an intercalation layer of LLTO and LMO with a thickness of about 5µm is evident, it is likely that only Mn ions and Ti ions interdiffused, while the La ions did not diffuse into the LMO. This agrees well with the EDS mapping

shown in Fig. 4(c). In the Ti element mapping, we observed an obvious Ti diffusion into the LMO, and similarly, manganese was also detected in the LLTO. On the other hand, lanthanum was not detected in the LMO. Similarly to the conventionally sintered sample, the true diffusion distances for Mn, Ti and La ions are in the order of 100-300μm and much larger than our scan length in Fig.5 (b) (Fig.S2 in supplementary information). Again, no evidence for a second phase was found in the line scan. These results on interdiffusion in the SPS sample agree well with those of the conventionally sintered sample. Thus, the interphase formation does not depend on the sintering technique, and an interphase containing manganese, titanium and oxygen is always formed at the LLTO/LMO interface during sintering.

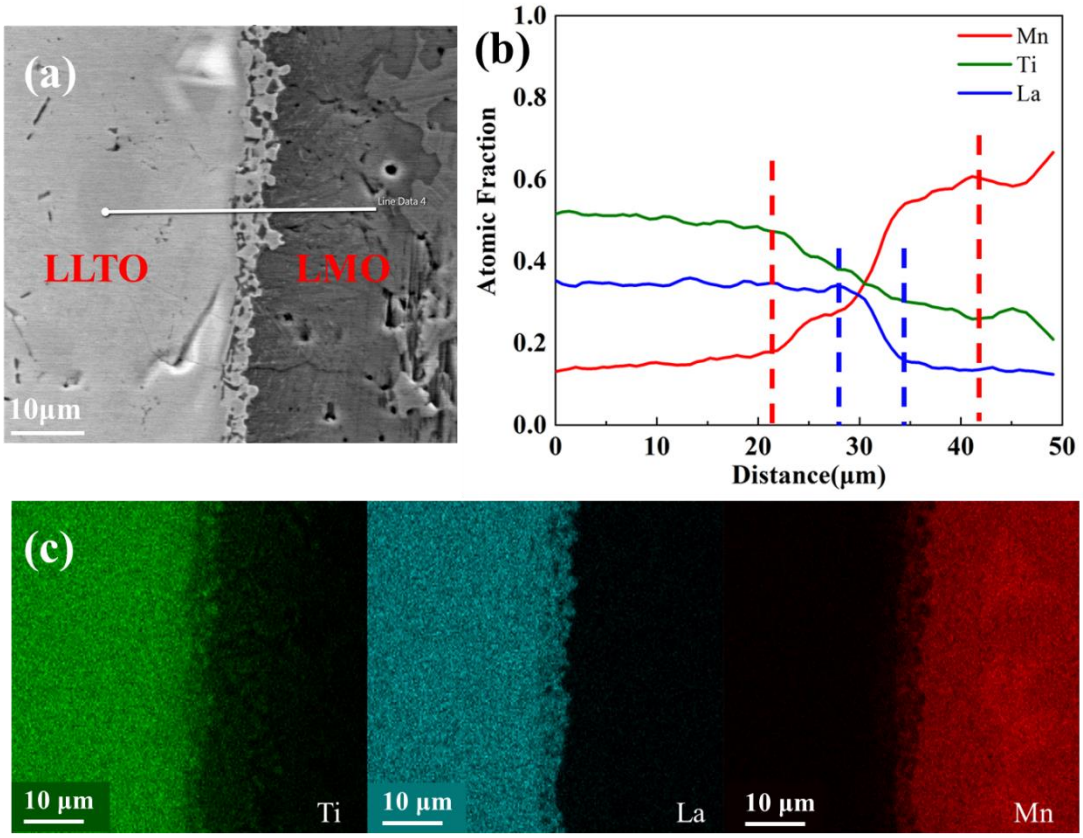

Figure 4 (a) Cross-sectional SEM image of SPS sintered sample. (b) Atomic fraction profile across the white line (from left to right) in (a), obtained by EDS line scan. (c) Element distribution profile of the region shown in (a), obtained by EDS mapping.

Additionally, by comparing the interfaces of the two samples, we have an intuitive understanding of the advantage of SPS over conventional sintering in battery processing. SPS densifies the LLTO/LMO layered samples better and provides better interfacial contact. This is mostly the effect of the pressure applied during sintering, as well as the electrical field effects that have been proven in literature to accelerate diffusion responsible for materials densification, especially in cases when, like in this work, there is a chemical potential difference present in the sample. The rapid heating rate of 100°C/min employed in the SPS sintering experiment presented here has also been shown to reduce grain growth during sintering, by bypassing the initial sintering stage where coarsening mechanisms are active, consuming driving force for densification[36]. Moreover, the pressure and the diffusion acceleration due to electrical field[31] also improves the contact between electrode/electrolyte, thus reducing the internal resistance of the SSBs.

To further confirm our results at a higher resolution level, a 20μm × 8μm rectangular lamella was cut and lifted out from the interfacial region by the FIB operation system (Fig.6 (a)). After that, the lamella was thinned to 100nm thickness and analyzed by high angle angular dark field (HAADF-STEM), and STEM-EDS in Fig.6 (b) and (c). According to the Z contrast of STEM-HAADF, we can identify that the brighter phase is LLTO and the darker phase is LMO. According to the needle-like structure, it is likely that during sintering at high temperature the region in red circle was a single phase that either decomposed due to decreasing solubilities or a phase transition during cooling. The EDS mapping in Fig.6 (c) confirmed that in the "mixture region", both Ti and Mn element were present, while the La element was again not detected. A needle-like distribution of Mn becomes evident. Fig.6 (d) and (e) provided a higher resolution mapping of this "needle-like" region. The upper third containing a bright phase in (d) is LLTO, while the darker region below contains two different phases with different contrast. These two phases (I, II) are different in Mn concentration with more Mn in brighter regions (I). We also observed a segregation of Mn around the Mn-deficient regions as indicated by a white arrow. Overall, the Ti concentration exhibited a distribution that is inverse to Mn, though at a lower extent. From these TEM results, the existence of an interphase formed by the interdiffusion between Mn ions and Ti ions was further confirmed.

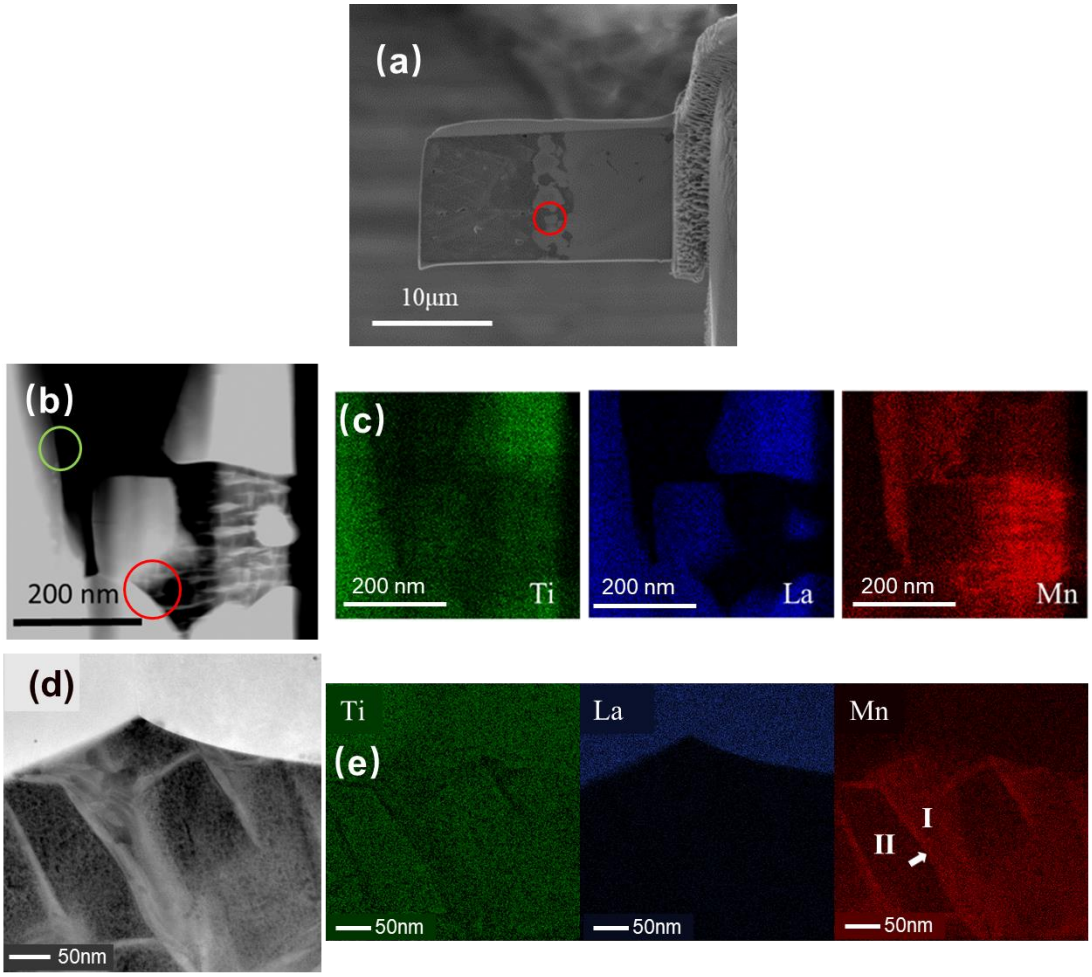

Figure 5 (a) Interfacial region obtained by focused ion beam (FIB) and lift-out. (b) STEM image of the circled region in (a). (c) Element distribution profile of (b) obtained by EDS mapping. (d) HAADF image of red circled region in (b). (e) Element distribution profile of (d), obtained by EDS mapping.

Figure 7 shows a high resolution TEM (HRTEM) image of the green circled region in Fig. 6 (b) where LMO and LLTO are in direct contact. According to this micrograph, an amorphous layer is present at the interface. The thickness of this layer is between 3 and 10 nm as the tilting angle of this layer is not known. Such amorphous films at interfaces are known as complexions[37,38] and are known to occur in various battery materials. [39–42] The complexion is a two-dimensional interfacial phase that is stabilized by its impact on the grain boundary energy. Potentially it affects the ion transportation across the interface drastically. In summary, at the LLTO/LMO interface, we observed two kinds of interphase. One is an interdiffusion layer with the thickness of tens of microns, formed by the interdiffusion between manganese and titanium. The other is an

amorphous complexion with the thickness of a few nanometers.

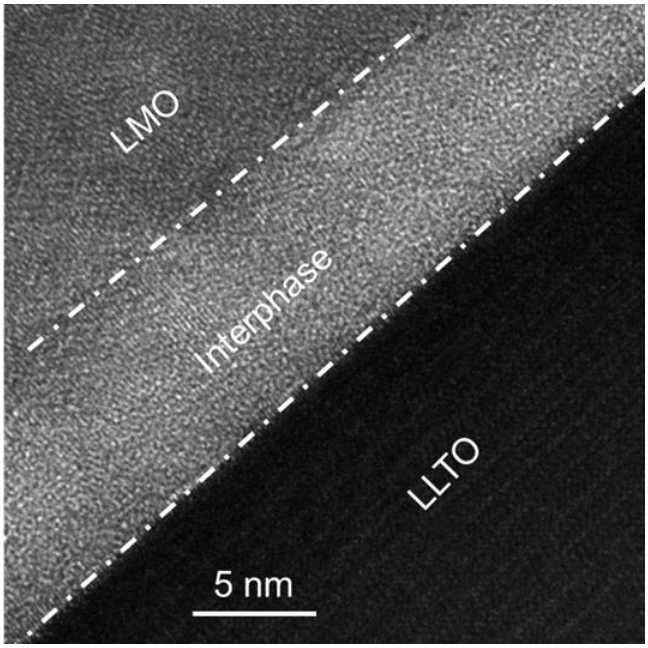

Figure 6 HRTEM image of the green circled region in Fig.6 (e).

Based on the results discussed above, the interphase between LLTO and LMO contains titanium, manganese and oxygen. Unfortunately, no information is available for lithium as it is not visible by EDS and the EELS technique, which could shed light on lithium presence, is not currently available at our institution. Element interdiffusion usually follows a substitutional diffusion mechanism. LLTO is a perovskite (ABO_3) type electrolyte, where La^{3+} cations sit at the A sites, with a coordination number of 12, and Ti^{4+} cations sit at the B sites, with a coordination number of 6. Meanwhile, LMO has a spinel structure (AB_2O_4), where manganese is a mixture of Mn^{3+} and Mn^{4+} states, and these cations and sit at the B sites (octahedral interstitial) , with a coordination number of six[43]. The ionic radii of these cations are: La^{3+}=150pm, Ti^{4+}=74.5pm, Mn^{3+}=72pm, and Mn^{4+}=67pm [44]. In substitutional diffusion, the smaller difference in ionic sizes, the smaller energy barrier ions need to overcome for diffusion to occur. As Ti^{4+} and Mn^{3+}/Mn^{4+} are very close in size and charge and the size of La^{3+} is much larger, it is reasonable that no diffusion of La ions occurs, while Mn and Ti ions form extended interdiffusion layers with a thickness of tens of μm.

Electrical Characterization of SPS Sample

In SSBs, the unwanted large interfacial resistance is likely to be caused by the interphase.[39] As the interphase layer is expected to have a high resistance, it can be identified in electrochemical impedance spectroscopy (EIS) as an additional part in the Nyquist plot, as reported in Koerver's work[16]. In general, separating individual contributions to the impedance of complex samples is challenging. In the present case, this is particularly true as the interphase even contains two different layers (i.e. the interdiffusion layer and the amorphous phase). In the present work, we compared the impedance of LLTO/LMO composite with that of LLTO and of LMO to separate the impedance of the interphase layer. Fig.8 (a) shows the impedance profile of SPS sintered LLTO (900°C, 10 minutes, 50 MPa). In general, the overall resistance of LLTO can be divided into two parts, the LLTO grain impedance and the grain boundary impedance. The grain contribution usually occurs at higher frequencies than the grain boundary contribution. Moreover, in the equivalent circuit in Fig.8 (a), a constant phase element has also been added to include the electrode/LLTO contact capacitance.[45] After fitting with the equivalent circuit (Fig.8 (a)) and adding the two resistances of the equivalent circuit (see table S3 in the supplementary information), the fitted bulk resistance of LLTO was found to be approximately 12,000Ω. The ionic conductivity can be calculated through the equation $\sigma = \rho\frac{l}{s}$ and was found to be approximately 1.1×10^{-5} S/cm, which is comparable with data from the literature[10]. Fig.8 (b) shows the impedance of LMO. Given that LMO possesses both electronic and ionic conductivity, we applied the equivalent circuit in Fig. 8 (b) [46] to fit the impedance data, and the fitting result was reasonable. Fig.8 (c) shows the impedance profile of the LLTO/LMO SPS co-sintered pellet. As this sample is a series of LMO and LLTO, the respective equivalent should be a series of those used for LLTO and LMO in Fig. 8 (a) and (b). For the interphase, at least one RC circuit should be added as shown in Fig.8 (e). However, this equivalent circuit results in a fitting function with 20 parameters which cannot be fitted to the data in a reasonable way. Accordingly, a simplified equivalent

circuit (Fig.8 (c)) was performed, with the LMO, LLTO and interphase parts in series. As Fig.8 (c) shows, the fitting result still did not give valuable information on the electric properties of the interphase. However, based on the fitted curve, we can estimate that the overall resistance of the co-sintered layered sample by adding the resistances of all three resistors in the equivalent circuit (Table S5 in the supplementary information). The estimated resistance of this interphase is about $1\times10^6\ \Omega$. This is much larger than the individual resistance of LLTO and LMO as shown in Fig.8 (d). This much higher resistance is most likely caused by the formation of the interphase as discussed in the previous section. However, the specific resistance for this interphase could not be evaluated by the fitting procedure shown in Fig. 8.

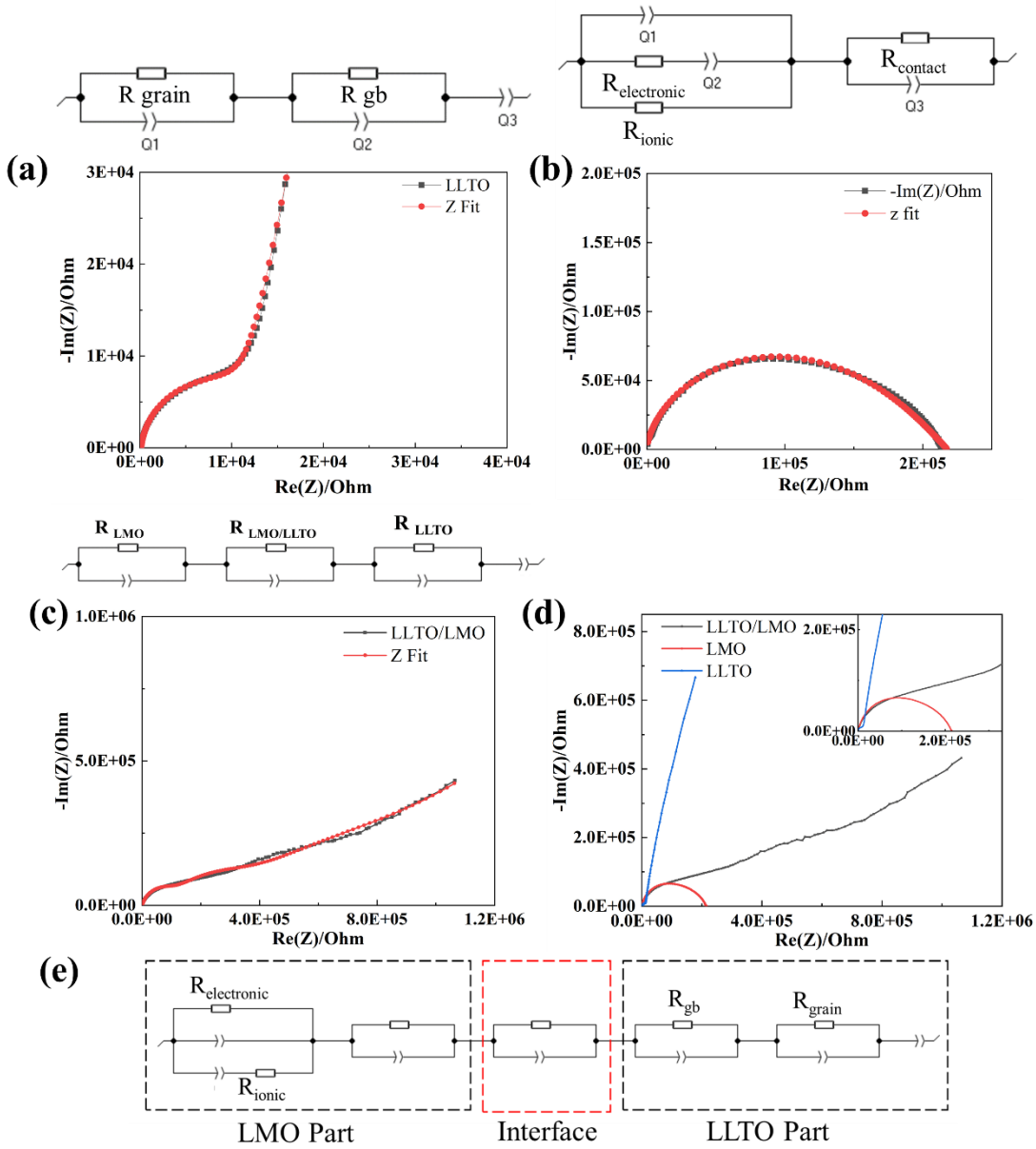

Figure 7 (a) The impedance profile of SPS sintered LLTO and the fitting result based on the equivalent circuit on the top. (b) The impedance profile of LMO and the fitting result base on equivalent circuit on the top. (c) The impedance profile of LLTO/LMO co-sintered by SPS and the fitted result based on the equivalent circuit on the top. (d) The overlaid impedance profiles of LLTO/LMO (black) LLTO (blue) and LMO (red). (e) Equivalent circuit of LLTO/LMO.

One way to approach the impedance of the interphase is to use the results from individual LLTO and LMO samples. As the LLTO/LMO is a series of these two materials and the interphase, the impedance of the interphase $Z_{interphase}$ corresponds to the difference between the individual impedances of LMO (Z_{LMO}) and LLTO (Z_{LLTO})

and the impedance of the LLTO/LMO ($Z_{LLTO/LMO}$) sample. Fig.9 (a) and (b) show a comparison of the measured $|Z|_{LLTO/LMO}$ (black curve) with the mathematical addition of $|Z|_{LMO}$ and $|Z|_{LLTO}$ (green curve). The gap between the black and green curve corresponds to a large interfacial resistance caused by the interphase. To analyze the impedance of the interphase, we estimated the imaginary part of interfacial impedance using the information on the impedance of separate LMO and LLTO samples:

$$Im(Z_{interphase})=Im(Z_{LLTO/LMO})-(Im(Z_{LLTO})+Im(Z_{LMO})). \quad (1)$$

Analogue, we estimate the real part of interfacial impedance by:

$$Re(Z_{interphase})=Re(Z_{LLTO/LMO})-(Re(Z_{LLTO})+Re(Z_{LMO})). \quad (2)$$

Subsequently, we plotted the Nyquist diagram ($-Im(Z_{interphase})$ vs $Re(Z_{interphase})$) from 10kHz to 5Hz as shown in Fig.9 (c). We have chosen this frequency range, as for higher frequencies, the difference between the black and green curve in Fig. 9 (a) is negligible indicating that the impedance of the interphase is negligible as well in that frequency range. For frequencies lower than 5Hz, the impedance data contains too much noise as evident in Fig. 8 (d). As the impedance of the interphase in Fig. 9 (c) clearly contains two semicircles, we used an equivalent circuit with two RC elements which provided a reasonable fit. From this fit, we were able to get an approximation of the resistance of the interphase with $R_1= 1.36\times10^5$ Ω, $R_2=3.3\times10^5$ Ω, $Q_1=2.42\times10^{-9}$ F ($a_1=1$) and $Q_2=1.58\times10^{-8}$ F ($a_2=1$). Accordingly, the interphase resistance was found to be 4.66×10^5 Ω, which is about 40 times higher than the overall resistance of the LLTO sample.

As for both constant phase elements Q_1 and Q_2, it was found that $a_1 = a_2 = 1$, Q_1 and Q_2 directly correspond to a capacity. Using a plate capacitor approach, the capacity is $C = \epsilon_0\epsilon_r A/d$ with the permittivity of the vacuum ϵ_0, the relative permittivity ϵ_r, the cross sectional area A and the layer thickness d. If we assume the relative permittivity to be in the order of 30 for LLTO and LMO, a layer thicknesses of ~10µm for Q_1 and ~1µm

for Q_2 is obtained. Considering the layer thicknesses known form electron microscopy for the interdiffusion layer (several tens of μm) and the amorphous film (~5nm), the high resistance of the interface seems not to stem from the nm thick amorphous film. Instead, the impedance data indicates that the interdiffusion layer is causing the high interphase resistance. This result agrees well with the literature as nanometer thick amorphous layers are known to enhance the transport of Li for certain cathode materials[39,42,47].

Overall, our results confirm that the high interfacial resistance between electrodes and electrolyte will play an important negative role in the performance of all-solid-state batteries. This is a significant challenge in the field of all solid state batteries, which has to be overcome by designing electrode/electrolyte pairs that are likely to bypass the formation of such interfacial layers with high resistance. In the light of the present study, research should focus particularly on hindering interdiffusion and not on preventing amorphous layer formation as the latter is not relevant for the high resistance of the interphase. Computational studies can aid materials selection, and finding new processing techniques that will encourage densification, while discouraging interphase layer formation are key pathways toward overcoming this roadblock.

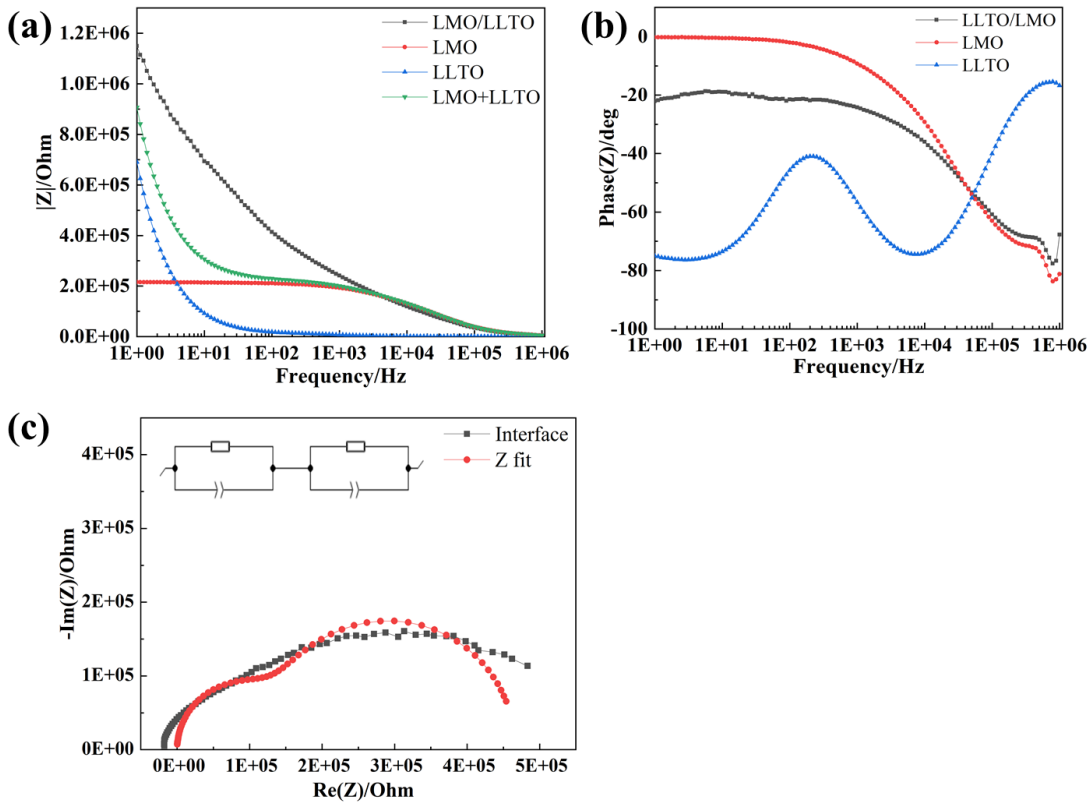

Figure 8 (a) plot of |Z| vs Frequency for LLTO/LMO (black), LMO (green), LLTO (blue), and the mathematical addition of LMO and LLTO. (b) Phase angle vs Frequency plot for LLTO/LMO, LLTO and LMO. (c) Nyquist plot of the interphase from 10kHz to 5 Hz, and the fitted curve based on the equivalent circuit above.

Conclusions

We studied the compatibility between the perovskite electrolyte material: $Li_{0.33}La_{0.57}TiO_3$(LLTO) and the spinel cathode material: $LiMn_2O_4$ (LMO) with respect to the formation of interfacial phases and their effect on electrical conductivity. We applied co-sintering experiments to the LLTO/LMO layered samples by both conventional sintering and spark plasma sintering (SPS). SPS sintering resulted in both denser samples and better interfacial contact. Moreover, we identified an amorphous complexion film formed at the LLTO/ LMO interface by HRTEM. We studied the interfacial composition with by analytical STEM and SEM and confirmed that the interphase contained manganese, titanium and oxygen. EIS characterization also indicated that the formation of this interphase greatly and negatively affected the ionic conductivity of the layered sample as the interfacial resistance is larger by a factor of about 40 compared to the individual phases. Interestingly, the amorphous layer at the grain boundary seems not to contribute to this high grain boundary resistance; the high impedance is only caused by the interdiffusion layer. Therefore, to improve the performance of SSBs, it is necessary to use predictive computational modelling to study the formation kinetics of the interphase in a library of all solid-state electrode/electrolyte combinations. The goal of these studies is to minimize interdiffusion resulting in the formation of an interphase with high resistivity or to engineer the interphase towards enhanced ionic conduction performance.

Reference

(1) Wen, J.; Yu, Y.; Chen, C. A Review on Lithium-Ion Batteries Safety Issues: Existing Problems and Possible Solutions. *Mater. Express* **2012**, *2* (3), 197–212.

(2) Manthiram, A.; Yu, X.; Wang, S. Lithium Battery Chemistries Enabled by Solid-State Electrolytes. *Nat. Rev. Mater.* **2017**, *2* (4), 1–16.

(3) Janek, J.; Zeier, W. G. A Solid Future for Battery Development. *Nat. Energy* **2016**, *1* (9).

(4) Yu, C.; Ganapathy, S.; Eck, E. R. H. V.; Wang, H.; Basak, S.; Li, Z.; Wagemaker, M. Accessing the Bottleneck in All-Solid State Batteries, Lithium-Ion Transport over the Solid-Electrolyte-Electrode Interface. *Nat. Commun.* **2017**, *8* (1), 1–9.

(5) Takada, K.; Ohno, T.; Ohta, N.; Ohnishi, T.; Tanaka, Y. Positive and Negative Aspects of Interfaces in Solid-State Batteries. *ACS Energy Lett.* **2018**, *3* (1), 98–103.

(6) Richards, W. D.; Miara, L. J.; Wang, Y.; Kim, J. C.; Ceder, G. Interface Stability in Solid-State Batteries. *Chem. Mater.* **2016**, *28* (1), 266–273.

(7) Li, Y.; Zhou, W.; Chen, X.; Lü, X.; Cui, Z.; Xin, S.; Xue, L.; Jia, Q.; Goodenough, J. B. Mastering the Interface for Advanced All-Solid-State Lithium Rechargeable Batteries. *Proc. Natl. Acad. Sci.* **2016**, *113* (47), 13313–13317.

(8) Yamada, H.; Suzuki, K.; Nishio, K.; Takemoto, K.; Isomichi, G.; Moriguchi, I. Interfacial Phenomena between Lithium Ion Conductors and Cathodes. *Solid State Ionics* **2014**, *262*, 879–882.

(9) Kamaya, N.; Homma, K.; Yamakawa, Y.; Hirayama, M.; Kanno, R.; Yonemura, M.; Kamiyama, T.; Kato, Y.; Hama, S.; Kawamoto, K.; et al. A Lithium Superionic Conductor. *Nat. Mater.* **2011**, *10* (9), 682–686.

(10) Inaguma, Y.; Liquan, C.; Itoh, M.; Nakamura, T.; Uchida, T.; Ikuta, H.; Wakihara, M. High Ionic Conductivity in Lithium Lanthanum Titanate. *Solid State Commun.* **1993**.

(11) Aono, H. Ionic Conductivity of Solid Electrolytes Based on Lithium Titanium Phosphate. *J. Electrochem. Soc.* **1990**.

(12) Bernuy-Lopez, C.; Manalastas, W.; Lopez Del Amo, J. M.; Aguadero, A.; Aguesse, F.; Kilner, J. A. Atmosphere Controlled Processing of Ga-Substituted Garnets for High Li-Ion Conductivity Ceramics. *Chem. Mater.* **2014**.

(13) Bachman, J. C.; Muy, S.; Grimaud, A.; Chang, H. H.; Pour, N.; Lux, S. F.; Paschos, O.; Maglia, F.; Lupart, S.; Lamp, P.; et al. Inorganic Solid-State Electrolytes for Lithium Batteries: Mechanisms and Properties Governing Ion Conduction. *Chem. Rev.* **2016**, *116* (1), 140–162.

(14) Gellert, M.; Dashjav, E.; Grüner, D.; Ma, Q.; Tietz, F. Compatibility Study of Oxide and Olivine Cathode Materials with Lithium Aluminum Titanium Phosphate. *Ionics (Kiel).* **2018**, *24* (4), 1001–1006.

(15) Kim, K. H.; Iriyama, Y.; Yamamoto, K.; Kumazaki, S.; Asaka, T.; Tanabe, K.; Fisher, C. A. J.; Hirayama, T.; Murugan, R.; Ogumi, Z. Characterization of the

Interface between LiCoO2 and Li 7La3Zr2O12 in an All-Solid-State Rechargeable Lithium Battery. *J. Power Sources* **2011**, *196* (2), 764–767.
(16) Koerver, R.; Aygün, I.; Leichtweiß, T.; Dietrich, C.; Zhang, W.; Binder, J. O.; Hartmann, P.; Zeier, W. G.; Janek, J. Capacity Fade in Solid-State Batteries: Interphase Formation and Chemomechanical Processes in Nickel-Rich Layered Oxide Cathodes and Lithium Thiophosphate Solid Electrolytes. *Chem. Mater.* **2017**, *29* (13), 5574–5582.
(17) Haruyama, J.; Sodeyama, K.; Han, L.; Takada, K.; Tateyama, Y. Space-Charge Layer Effect at Interface between Oxide Cathode and Sulfide Electrolyte in All-Solid-State Lithium-Ion Battery. *Chem. Mater.* **2014**, *26* (14), 4248–4255.
(18) Takada, K. Progress and Prospective of Solid-State Lithium Batteries. *Acta Mater.* **2013**, *61* (3), 759–770.
(19) Han, F.; Yue, J.; Chen, C.; Zhao, N.; Fan, X.; Ma, Z.; Gao, T.; Wang, F.; Guo, X.; Wang, C. Interphase Engineering Enabled All-Ceramic Lithium Battery. *Joule* **2018**, *2* (3), 497–508.
(20) Sakuda, A.; Hayashi, A.; Tatsumisago, M. Interfacial Observation between LiCoO2 Electrode and Li 2S-P2S5 Solid Electrolytes of All-Solid-State Lithium Secondary Batteries Using Transmission Electron Microscopy. *Chem. Mater.* **2010**, *22* (3), 949–956.
(21) Uhlenbruck, S.; Dornseiffer, J.; Lobe, S.; Dellen, C.; Tsai, C.; Gotzen, B.; Sebold, D.; Finsterbusch, M.; Guillon, O. Cathode-Electrolyte Material Interactions during Manufacturing of Inorganic Solid-State Lithium Batteries. **2017**, 197–206.
(22) Ohta, S.; Seki, J.; Yagi, Y.; Kihira, Y.; Tani, T.; Asaoka, T. Co-Sinterable Lithium Garnet-Type Oxide Electrolyte with Cathode for All-Solid-State Lithium Ion Battery. *J. Power Sources* **2014**, *265*, 40–44.
(23) Miara, L.; Windmuller, A. About the Compatibility between High Voltage Spinel Cathode Materials and Solid Oxide Electrolytes as a Function of Temperature. **2016**.
(24) Ren, Y.; Chen, K.; Chen, R.; Liu, T.; Zhang, Y.; Nan, C. W. Oxide Electrolytes for Lithium Batteries. *J. Am. Ceram. Soc.* **2015**, *98* (12), 3603–3623.
(25) Stramare, S.; Thangadurai, V.; Weppner, W. Lithium Lanthanum Titanates: A Review. *Chem. Mater.* **2003**, *15* (21), 3974–3990.
(26) Yao, X.; Huang, B.; Yin, J.; Peng, G.; Huang, Z.; Gao, C.; Liu, D.; Xu, X. All-Solid-State Lithium Batteries with Inorganic Solid Electrolytes: Review of Fundamental Science. *Chinese Phys. B* **2015**, *25* (1), 1–14.
(27) Bachman, J. C.; Muy, S.; Grimaud, A.; Chang, H.; Pour, N.; Lux, S. F.; Paschos, O.; Maglia, F.; Lupart, S.; Lamp, P.; et al. Inorganic Solid-State Electrolytes for Lithium Batteries : Mechanisms and Properties Governing Ion Conduction. **2016**.
(28) Gummow, R. J.; Kock, A. De; Thackeray, M. M. Improved Capacity Retention in Rechargeable 4 V Lithium/Lithiummanganese Oxide (Spinel) Cells. *Solid State Ionics* **1994**, *2738* (94).
(29) Kobayashi, Y. All-Solid-State Lithium Secondary Battery with

Ceramic/Polymer Composite Electrolyte. *Solid State Ionics* **2002**, *152–153*, 137–142.

(30) Guillon, O.; Gonzalez-Julian, J.; Dargatz, B.; Kessel, T.; Schierning, G.; Räthel, J.; Herrmann, M. Field-Assisted Sintering Technology/Spark Plasma Sintering: Mechanisms, Materials, and Technology Developments. *Adv. Eng. Mater.* **2014**, *16* (7), 830–849.

(31) Ya, M. O. H. N. A. G. I. The Effect of Electric Field and Pressure on the Synthesis and Consolidation of Materials : A Review of the Spark Plasma Sintering Method. **2006**, *1*, 763–777.

(32) Kali, R.; Mukhopadhyay, A. Spark Plasma Sintered / Synthesized Dense and Nanostructured Materials for Solid-State Li-Ion Batteries : Overview and Perspective. *J. Power Sources* **2014**, *247*, 920–931.

(33) Kobayashi, Y.; Takeuchi, T.; Tabuchi, M.; Ado, K.; Kageyama, H. Densification of LiTi 2 ž PO 4 / 3 -Based Solid Electrolytes By. **1999**.

(34) Li, J.; Doig, R.; Camardese, J.; Plucknett, K.; Dahn, J. R. Measurements of Interdiffusion Coefficients of Transition Metals in Layered Li-Ni-Mn-Co Oxide Core-Shell Materials during Sintering. *Chem. Mater.* **2015**, *27* (22), 7765–7773.

(35) Kim, K. H.; Iriyama, Y.; Yamamoto, K.; Kumazaki, S.; Asaka, T.; Tanabe, K.; Fisher, C. A. J.; Hirayama, T.; Murugan, R.; Ogumi, Z. Characterization of the Interface between LiCoO2and Li7La3Zr2O12in an All-Solid-State Rechargeable Lithium Battery. *J. Power Sources* **2011**, *196* (2), 764–767.

(36) García, D. E.; Seidel, J.; Janssen, R.; Claussen, N. Fast Firing of Alumina. *J. Eur. Ceram. Soc.* **1995**.

(37) Cantwell, P. R.; Tang, M.; Dillon, S. J.; Luo, J.; Rohrer, G. S.; Harmer, M. P. Grain Boundary Complexions. *Acta Mater.* **2014**.

(38) Luo, J. Stabilization of Nanoscale Quasi-Liquid Interfacial Films in Inorganic Materials: A Review and Critical Assessment. *Crit. Rev. Solid State Mater. Sci.* **2007**.

(39) Luo, J. Interfacial Engineering of Solid Electrolytes. *J. Mater.* **2015**, *1* (1), 22–32.

(40) Mei, A.; Wang, X. L.; Lan, J. Le; Feng, Y. C.; Geng, H. X.; Lin, Y. H.; Nan, C. W. Role of Amorphous Boundary Layer in Enhancing Ionic Conductivity of Lithium-Lanthanum-Titanate Electrolyte. *Electrochim. Acta* **2010**.

(41) Ma, C.; Chen, K.; Liang, C.; Nan, C. W.; Ishikawa, R.; More, K.; Chi, M. Atomic-Scale Origin of the Large Grain-Boundary Resistance in Perovskite Li-Ion-Conducting Solid Electrolytes. *Energy Environ. Sci.* **2014**.

(42) Kayyar, A.; Qian, H.; Luo, J. Surface Adsorption and Disordering in LiFePO 4 Based Battery Cathodes. *Appl. Phys. Lett.* **2009**.

(43) Chiang, Y.-M.; Birnie, D. P.; Kingery, W. D. *Physical Ceramics*; 1997.

(44) Barsoum, M. W. *Fundamentals Of Ceramics*; 2003.

(45) Wu, J.-F.; Guo, X. Origin of the Low Grain Boundary Conductivity in Lithium Ion Conducting Perovskites: $Li_{3x}La_{0.67-x}TiO_3$. *Phys. Chem. Chem. Phys.* **2017**, *19* (8), 5880–5887.

(46) Huggins, R. A. *Advanced Batteries: Materials Science Aspects*; 2009.
(47) Kang, B.; Ceder, G. Battery Materials for Ultrafast Charging and Discharging. *Nature* **2009**.